EFFECTS OF MOTION ESTIMATION METHODS ON 4D GATED CARDIAC SPECT RECONSTRUCTION

Wenyuan Qi, *Xiaofeng Niu*, and *Yongyi Yang*

Department of Electrical and Computer Engineering, Illinois Institute of Technology
3301 S. Dearborn Street, Chicago, IL 60616, USA

ABSTRACT

Cardiac gated SPECT imaging suffers from several degrading factors including limited data counts, depth-dependent blur, attenuation, scatter, and motion blur. In recent work we demonstrated that use of temporal processing could lead to the most improvement in 4D reconstruction. In this work we investigate how motion estimation models can affect the reconstruction in 4D, and in particular, we examine how much room is still left in optical flow estimation toward improving the image quality of reconstruction. In our experiments we conducted a thorough, quantitative evaluation using simulated imaging study with multiple noise realizations from the NCAT phantom. As an upper bound, the known motion from NCAT was used for reconstruction. The results show that 4D reconstruction with a periodic optical flow model can achieve results almost matching that with the known motion.

***Index Terms*—**Optical flow, motion estimation, spatio-temporal processing, gated cardiac SPECT.

1. INTRODUCTION

In nuclear cardiology, single photon emission computed tomography (SPECT) plays an important role for detection and evaluation of coronary artery disease. Besides myocardial perfusion, gated SPECT can also provide valuable functional information such as ejection fraction, wall motion and wall thickening [1]. In gated SPECT, the cardiac cycle is divided into several time intervals according to the ECG signal, and an image is reconstructed for each interval. However, gated SPECT images also suffer from a number of degrading factors, including limited data counts, depth-dependent blur, attenuation, scatter, and motion blur [2].

In recent years there have been several different methods studied to improve reconstruction in gated imaging by exploiting the correlation in the signal components among different gated frames, e.g. [3-5]. In [6] we developed a spatio-temporal (4D) reconstruction approach for gated images, wherein a temporal prior was defined to enforce smoothing among temporally neighboring frames in a gated sequence. Subsequently in [7], we investigated the effects of various degrading factors on the reconstructed images by several representative reconstruction algorithms. It is observed that, compared to other factors, use of temporal processing in 4D reconstruction can lead to the most improvement in gated images.

A key issue with temporal processing in 4D reconstruction is the use of a temporal prior. Ideally, this temporal prior should enforce smoothing along the trajectories of cardiac motion in order to avoid motion blur. However, in practice this motion information is not readily available, and has to be estimated from the image data. For example, in [8] a joint framework was proposed in which both image reconstruction and motion estimation were carried out simultaneously in an alternating fashion.

Because of the importance of temporal processing in 4D reconstruction, recently in [9] we applied a periodic model to regularize the optical flow (i.e., the apparent image motion) among the temporal frames in a gated sequence, of which the purpose is to improve the estimation of the optical flow in the temporal prior. It was demonstrated that this periodic model could improve the accuracy of the 4D reconstruction [10]. In this work we conduct a comparison study on the effects of optical flow estimation on 4D reconstruction. In particular, we ask the following important question: *how much more room is still left in optical flow estimation toward improving the quality in 4D reconstruction*?

Toward this goal, we use simulated imaging study with multiple noise realizations using the NURBS-based cardiac-torso (NCAT) phantom [11]. We apply two sets of NCAT phantom data with different patient geometry, one male and one female, of which the latter has significantly higher breast and diaphragmatic attenuation; for lesion detection, perfusion defects of different sizes, contrasts, and locations are introduced in the phantoms. As an upper bound for comparison, we also apply in 4D reconstruction the known motion derived from NCAT.

In the experiments, we conduct a thorough quantitative evaluation of the reconstructed myocardium using a number of metrics: 1) overall noise level of the left ventricular (LV) myocardium, 2) regional accuracy of the LV through bias-variance analyses and time activity curves (TACs), 3) perfusion lesion detectability quantified by a channelized Hotelling observer (CHO) [12]. Furthermore, as an indicator

This work was supported by NIH/NHLBI Grant HL65425.

of distortion in the reconstructed LV wall, we also examine the shape of the LV wall by detecting its contours.

2. METHODS

2.1 4D reconstruction of gated SPECT

In gated cardiac SPECT, the acquired projection data are binned into *K* cardiac intervals according ECG signal. The imaging data are described by the following model:

$$E[g_k] = Hf_k, k = 1,..., K \quad (1)$$

where g_k and f_k are vectors representing the acquired data (sinogram) and original image, respectively, in gate k, H is the system matrix describing the imaging process, and $E[\cdot]$ is the expectation operator.

For convenience, let $F \equiv (f_1^T, f_2^T, ..., f_K^T)^T$, i.e. a vector consisting of all the gate frames; similarly, let $G \equiv (g_1^T, g_2^T, ..., g_K^T)^T$. Then, the maximum *a posteriori* (MAP) estimate of F is obtained as:

$$\hat{F} \equiv \arg\max_F [\log p(G;F) + \log p(F)] \quad (2)$$

where $p(G;F)$ is the likelihood function of G parameterized by F, and $p(F)$ is a prior distribution on F. We assume a Poisson likelihood function $p(G;F)$ for the noise in SPECT. The prior $p(F)$ is defined as:

$$p(F) \propto \exp(-\beta_s U_s(F) - \beta_t U_t(F)) \quad (3)$$

where $U_s(F)$ and $U_t(F)$ are two energy functions defined in space and time, respectively, and β_s and β_t are their corresponding scalar weighting parameters. The temporal term $U_t(F)$ is defined according to the estimated image motion among the different gates [6].

2.2 Image motion models

For comparison, we consider motion vectors obtain from the following three sources for 4D reconstruction: 1) Horn-Schunck method [13], 2) periodic optical flow [10], and 3) motion derived from NCAT. For convenience, below we briefly describe them using the notion of 2D images, though our actual implementation is in 3D in the experiments.

a) Horn-Schunck optical flow

Consider an image sequence $I(x, y, t)$, where t denotes time and (x, y) denotes a spatial location in the image domain D. Let (u, v) denote the displacement vector of point (x, y) from time frame t to $(t+1)$. The Horn-Schunk's method determines the optical flow vectors through minimization of the following objective function:

$$E(u,v) = E_1(u,v) + \alpha E_2(u,v) \quad (4)$$

where

$$E_1(u,v) = \int_D (I(x,y,t) - I(x+u, y+v, t+1))^2 dxdy \quad (5)$$

and

$$E_2(u,v) = \int_D \left(|\nabla u|^2 + |\nabla v|^2 \right) dxdy . \quad (6)$$

In (4), the first term is based on the assumption that the image intensity at a point is constant along its motion trajectory, and the second term is used to regularize the spatial smoothness of the motion field. The parameter α is used to control the trade-off between these two terms.

b) Periodic optical flow

Consider $I(x, y, t)$ a periodic sequence, that is, $I(x, y, 0) = I(x, y, T)$. We aim to seek a simultaneous estimation procedure for the optical flow across the different frames in the sequence. To explicitly exploit the inherent periodicity in image motion, we model the motion components (u, v) at location (x, y) over time *t* as

$$\begin{aligned} u(x,y,t) &= \sum_{l=1}^{N} [a_l(x,y)\cos\omega_l t + b_l(x,y)\sin\omega_l t] \\ v(x,y,t) &= \sum_{l=1}^{N} [c_l(x,y)\cos\omega_l t + d_l(x,y)\sin\omega_l t] \end{aligned} \quad (7)$$

where a_l, b_l, c_l and d_l are the coefficients associated with harmonic component l, $\omega_l = 2\pi l/T$, and N is the number of harmonics used.

The unknown coefficients in (7) are determined through minimization of the objective function in (4), except that the two terms are now redefined as:

$$E_1(u,v) = \sum_{t=0}^{T-1} \int_D (I(x,y,t) - I(x+u, y+v, t+1))^2 dxdy \quad (8)$$

$$E_2(u,v) = \sum_{t=0}^{T-1} \int_D \left(|\nabla u| + |\nabla v| \right) dxdy . \quad (9)$$

Note that L_1 norm is used in (9) in order to exploit the piece-wise smoothness property in the motion field associated with the different organs.

c) Known motion from NCAT

In the NCAT phantom the motion trajectories of a set of predefined points on the heart wall are given over the different gated periods. We applied barycenter with distance weighting to obtain the vectors at the integer voxel locations on the heart wall.

2.3 Simulated imaging data

In our experiments, the 4D NCAT 2.0 phantoms [11] was used to generate the source and attenuation distribution. The SIMIND Monte Carlo package [14] was used to simulate gated SPECT imaging with Tc-99m labeled Sestamibi as the imaging agent and with the Picker Prism3000 with low-energy high-resolution (LEHR) collimator as the imaging system. The projection matrix was 64 by 64 with a pixel size 0.634cm. 64 projection sets were collected for each gated frame of total 16 gates. Two energy windows were used: the photopeak window was 20% (28 keV) centered at 140 keV, and a 3.5 keV window abutted to the lower side of the photopeak window for scatter correction. Poisson noise was introduced at a level of 8 million total acquired counts as in a typical clinical acquisition for a Tc-99m labeled Sestamibi study.

Two versions of the NCAT phantom, one male and one female were generated; a transverse slice is shown in Fig. 1

for each phantom. Note that the female phantom was generated with the same body size as the male but with a smaller rib size; thus, it has more significant breast and diaphragmatic attenuation. For each phantom, two datasets were generated, one with a lesion and the other without. For the two phantoms the perfusion defects were introduced at different regions of the LV (shown in Fig. 2(a) and (b)) with different sizes and contrasts (20% and 50% intensity reductions for male and female phantoms respectively). Each dataset included 30 noise realizations. There is also a high concentration of activities in the liver. For attenuation correction the corresponding attenuation map from each NCAT phantom was used.

For motion estimation, the images were first pre-reconstructed with spatial smoothing alone (i.e., 4D without temporal smoothing). Afterward the different motion estimation algorithms were applied to determine the motion from these resulting images, which were subsequently used for 4D reconstruction.

As reference, the gated images were also reconstructed from the noiseless projection data (without attenuation and scatter) using the OSEM algorithm. These images represent the ideal case of what would be obtained if the imaging system were free from these degrading factors.

2.3 Evaluation methods

To quantify the overall accuracy of the reconstructed myocardium, we compute the mean squared error (MSE) of a volumetric region containing the entire myocardium. We also quantify the regional accuracy of the LV wall by conducting bias-variance analyses on two selected regions of interest (ROI) on the LV (one normal and one defect, as shown in Fig. 2).

Furthermore, to demonstrate the effect of temporal smoothing on cardiac motion, we also calculate the time-activity curve (TAC) of an ROI near the base of the LV. As the wall moves in and out of this ROI, the image intensity of the ROI will vary accordingly. Thus, its TAC serves as a good indicator on the degree of temporal smoothing.

To quantify the detectability of the perfusion defect, we apply the CHO to a slice of the myocardium at the first gate interval (near end diastole) (Fig. 2). The performance is summarized using the area under the ROC curve (Az).

Finally, we also examine the distortion in the shape of the LV wall by detecting its contours with the Laplacian detector. These contours are used as an indicator of the amount of distortion associated with wall motion in the reconstructed images.

3. RESULTS

In Fig. 3, we show the MSE results from the two phantoms obtained with different motion models. Each curve is obtained by varying β_t as in (3), and $\beta_s = 0$ (such a choice was based on the optimal results in [7]). It can be seen that the known motion yields the smallest MSE in both phantoms. However, the periodic model TV-DFT-OFE could achieve almost a similar MSE level as the known motion. Note that the MSE level is higher in Fig. 3(b) than in Fig. 3(a), thanks to the significant breast and diaphragmatic attenuation in the female phantom

In Fig. 4, we show the bias-standard deviation plots of the normal ROI in the two phantoms obtained with different motion models. In these plots, each curve was obtained by varying β_t as in Fig. 3. All these results were obtained from 30 noise realizations. It is observed that at a same variance level the periodic model TV-DFT-OFE achieves a lower bias compared to OFE.

In Fig. 5 we show the CHO results from the two phantoms. These results show that TV-DFT-OFE achieves higher defect detectability than OFE in both cases. This is particularly more evident in the female phantom, where the lesion detectability with TV-DFT-OFE is almost as good as that with known motion. Interestingly, this is also consistent with the bias-standard deviation results in Fig. 4(b), where the result of TV-DFT-OFE is also similar to that of the known motion.

In Table I we show the cross-correlation coefficients between the reconstructed TACs and the ideal TAC of the TAC ROI (Fig. 2) obtained by different motion models. As can be seen, TV-DFT-OFE yields results much closer to that of the known motion than OFE.

In Fig. 6, we show the contours of a section of the LV in the reconstructed image of one gate (gate #1) by the different motion models. For reference, Fig. 6 (a) is the contour detected from the ideal reconstruction. Figs. 6 (b)-(d) are the contours of the same section obtained from 30 noise realizations with different motion models. There is larger degree of variation over the different noise realizations observed with OFE; the TV-DFT-OFE contours exhibit good agreement with that of known motion.

4. CONCLUSIONS

In this work, we studied the effects of different motion models on 4D reconstruction in cardiac gated SPECT. As an upper bound, we used reconstruction with known motion in order to examine how much more room is still left in optical flow estimation in terms of improving the quality in 4D reconstruction. We used NCAT phantoms with two different patient geometry and different perfusion defects in the experiments. The results show that the periodic motion model TV-DFT-OFE can achieve almost as good reconstruction accuracy and defect detectability as the known motion. Encouraged by these results, we plan to further evaluate TV-DFT-OFE in 4D using clinical acquisitions in the future.

5. REFERENCES

[1] E. G. Garcia, "Image guidelines for nuclear cardiology procedures part I," *J. Nucl. Card.*, vol. 3, pp. G1-G46, 1996.

[2] M. A. King, S. J. Glick, *et al*, " Attenuation, scatter, and spatial resolution compensation in SPECT," in *Emission Tomography: The Fundamentals of PET and SPECT*, edited by M. N. Wernick and J. N. Aarsvold (Elsevier Academic, London, 2004), Chap. XXII, pp. 473-498.

[3] D. S. Lalush and B. M. W. Tsui, "Block-iterative techniques for fast 4D reconstruction using a prior motion models in gated cardiac SPECT," *Phys. Med. Biol*., vol 43, pp. 875-886, 1998

[4] E. Gravier, Y. Yang and M. Jin, "Tomographic reconstruction of dynamic cardiac image sequences," *IEEE Trans. Img. Proc.*, vol. 16, no.4, 2007.

[5] J. G. Brankov, Y. Yang, and M. N. Wernick, "Spatio-temporal processing of gated cardiac SPECT images using deformable mesh modeling," *Med. Phys*., vol. 32, no. 9, pp. 2839-2849, 2005.

[6] E. Gravier and Y. Yang, "Motion-compensated reconstruction of tomograpic image sequences," *IEEE Trans. Nucl. Sci*., vol. 52, pp. 51056, 2005.

[7] X. Niu, Y. Yang, M. Jin, et. al, "Effects of motion, attenuation, and scatter corrections on gated cardiac SPECT reconstruction." *Med. Phys.*, 2011, accepted.

[8] Dr. R. Gilland, B. A. Mair, *et al*, "Simultanous reconstruction and motion estimation for gated cardiac ECT," *IEEE Trans. Nucl. Sci*., vol. 49, pp. 2344-2349,2002.

[9] L Li, Y Yang. "Optical Flow Estimation for a Periodic Image Sequence." *IEEE Trans. Img. Proc.* 19(1): 1-10 (2010)

[10] W. Qi, X. Niu and Y. Yang, "An improved periodic optical flow model for cardiac gated image reconstruction," *ISBI* 2011:1276-1279.

[11] W.P. Segars, *Development of a new dynamic NURBS-based cardiac-torso (NCAT) phantom*, Ph.D. thesis, The University of North Carolina, 2001.

[12] K. Myers and H. Barett, "Addition of a channel mechanism to the ideal-observer model," *J. Opt. Soc. Am.* JOSA A 4(12), pp. 2447-57, 1987.

[13] B.K.P. Horn and B.G. Schunck, "Determining optical flow," *Artificial Intelligence*, vol. 17, pp. 185-203, 1981.

[14] M. Ljungberg and S. V. Srand, "A Monto Carlo program simulating scintillation camera imaging," *Comp. Meth. Prog. Biomed.*, vol. 29, pp. 257-272, 1989.

Table 1. Cross-correlation coefficients between reconstructed and Ideal TACs from 30 noise realizations.

Methods	Male		Female	
	Mean	Std	Mean	Std
OFE	0.7761	0.0884	0.8067	0.1102
TV-DFT-OFE	0.9139	0.0509	0.8478	0.1033
Known	0.9631	0.0362	0.9243	0.0500

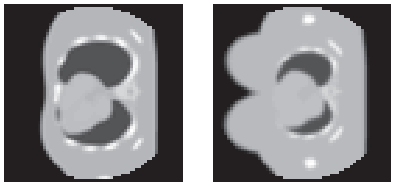
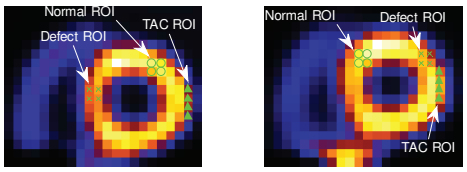
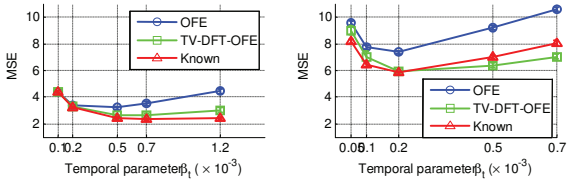


Fig. 1 Transverse slices of male (left) and female (right) phantoms.



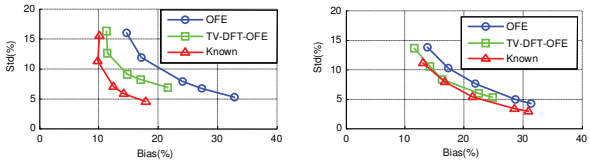
(a) Male (b) Female

Fig. 2 Regions of interests (ROIs) defined for bias-variance, CHO, and TAC metrics.



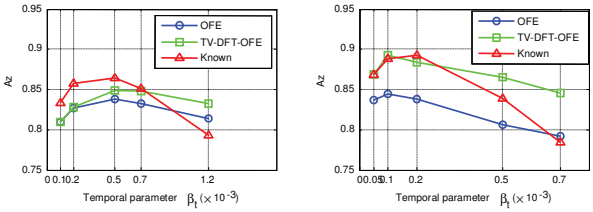
(a) Male (b) Female

Fig.3 MSE of the reconstructed myocardium obtained from 30 noise realizations.



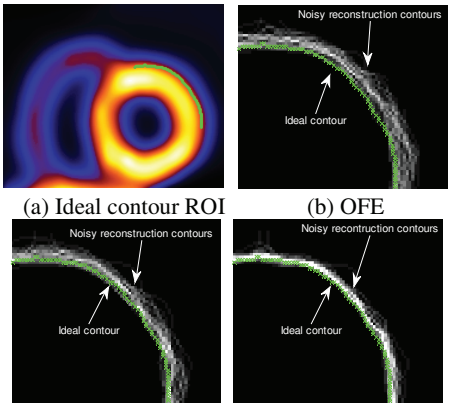
(a) Male (c) Female

Fig.4 Bias-standard deviation plots for the normal ROIsfrom 30 noise realizations.



(a) Male (b) Female

Fig. 5 CHO detection results of reconstruction with different motion estimation methods.



(a) Ideal contour ROI (b) OFE

(c) TV-DFT-OFE (d) Known

Fig. 6 Contour plot of reconstructed LV by different motion models.